

# Finite Element Modeling of a Silicon Tactile Sensor

Joseph Garvey, David Beebe<sup>1</sup> and Denice D. Denton<sup>2</sup>

Sentry Equipment, 856 East Armour Road, Oconomowoc, WI 53066, USA

<sup>1</sup>Department of Electrical and Computer Engineering, The Beckman Institute,  
University of Illinois at Urbana-Champaign, 405 North Mathews Ave, Urbana, IL 61801, USA

<sup>2</sup>Department of Electrical Engineering, University of Washington, Seattle, WA 98195, USA

(Received October 30, 1995; accepted February 18, 1997)

**Key words:** finite element modeling, silicon, tactile sensor, piezoresistive, diaphragm

Finite element modeling of a silicon tactile sensor is performed. The sensing element is based on a silicon diaphragm structure. Design characteristics such as over force protection, diaphragm thickness, and construction with differing materials are discussed. Three finite element models are developed: an axisymmetric, a 3-D, and a 3-D model with a force transmission structure. The effects of different load shapes and angles on the 3-D model are studied. The 3-D finite element model results are used for calculating the output voltage from the Wheatstone bridge and are compared with the output of a prototype sensor. Conclusions on the validity of the model are drawn.

## 1. Introduction

Micromachined silicon sensors are popular because they are compact, reliable, and can be mass produced. There is a pressing need in biomedical fields for a tactile sensor with these qualities.<sup>(1,2)</sup> Sensors used in tactile applications tend to be more complicated to manufacture than standard force/pressure sensors because of criteria such as skinlike packaging and durability. Requirements for a tactile sensor include skinlike properties, good durability, over force protection and small size, which enables its incorporation into arrays.<sup>(3)</sup>

Tufte *et al.* studied a silicon pressure sensitive piezoresistive diaphragm.<sup>(4)</sup> In their study they compared experimental results with results calculated using piezoresistive properties of silicon and the theory of uniformly loaded circular plates. Clark and Wise expanded on the earlier work by conducting a detailed analysis including a finite difference

numerical solution of diaphragm displacement and stress.<sup>(5)</sup> These early papers studied the interaction between the mechanical and the electrical operation of the silicon sensor. Advantages of the silicon sensor include no hysteresis or creep problems and over force protection.<sup>(6)</sup> Further work with silicon pressure sensors and micromachining has produced tactile sensors specifically tailored for biomedical applications.<sup>(7-9)</sup> Other structures developed for biomedical pressure sensors include those with a center boss or resonant strain gauges.<sup>(10,11)</sup> Different types of tactile sensors such as capacitive, piezoresistive and resonant strain gauges have been studied.<sup>(12)</sup> New design methods and types are aimed at producing sensors with increased output repeatability, better accuracy, or application-specific requirements. Advances in integrated circuit technology have made the silicon sensor producible in high volumes at low cost. New technology and further downsizing have resulted in high-density force measurement arrays for robotics and tactile imaging.<sup>(12,13)</sup>

In this paper we report the use of finite element modeling (FEM) in the design of a silicon tactile sensor encased in a flexible polyimide based package. The sensor is based on a silicon diaphragm structure with four implanted resistors arranged in a Wheatstone bridge configuration. Micromachining technologies including silicon direct bonding and bulk micromachining are used to fabricate the sensor. The sensor and leads are then encased in a flexible package to simulate skinlike properties and improve robustness. Three different FEM models are developed. The characteristics studied using the models include diaphragm displacement, stress across the surface of the diaphragm, and bridge output. Model accuracy and design considerations are discussed.

## 2. Sensor Fabrication

A thorough discussion of the packaging materials, package/sensor fabrication and package durability is presented elsewhere and will not be discussed in detail.<sup>(7,14)</sup> By utilizing silicon-to-silicon bonding and carefully controlling the depth of the reference chamber, a diaphragm structure can be fabricated which is intrinsically protected from breakage even under large loads.<sup>(15,16)</sup> Such a structure is shown in Fig. 1(a).

At this point, the sensor is functional as a pressure sensor only. The output of a pressure sensor is sensitive to the contact area (size) of the applied load. For tactile sensing applications, it is desirable to create a force sensor. A force sensor will yield a consistent output for equivalent load magnitudes regardless of the surface area of the applied load. In order to convert the pressure sensor to a force sensor, a force transmission structure in the shape of a dome was added to the sensor as shown in Fig. 1(b). The dome provides consistent outputs regardless of shape or size of the load. The dome acts to distribute the force over the entire diaphragm (i.e., it acts as a force transmission structure). A detailed cross-sectional view of the complete sensing element is shown in Fig. 1(c). To realize a flexible package the final fabrication step is an isotropic etch that removes the majority of the silicon leaving silicon buttons on a flexible polyimide skin. Note the curved edge profile caused by the final isotropic etch. Each sensor contains two silicon buttons. One button provides structural support for connector attachment, while the other button con-

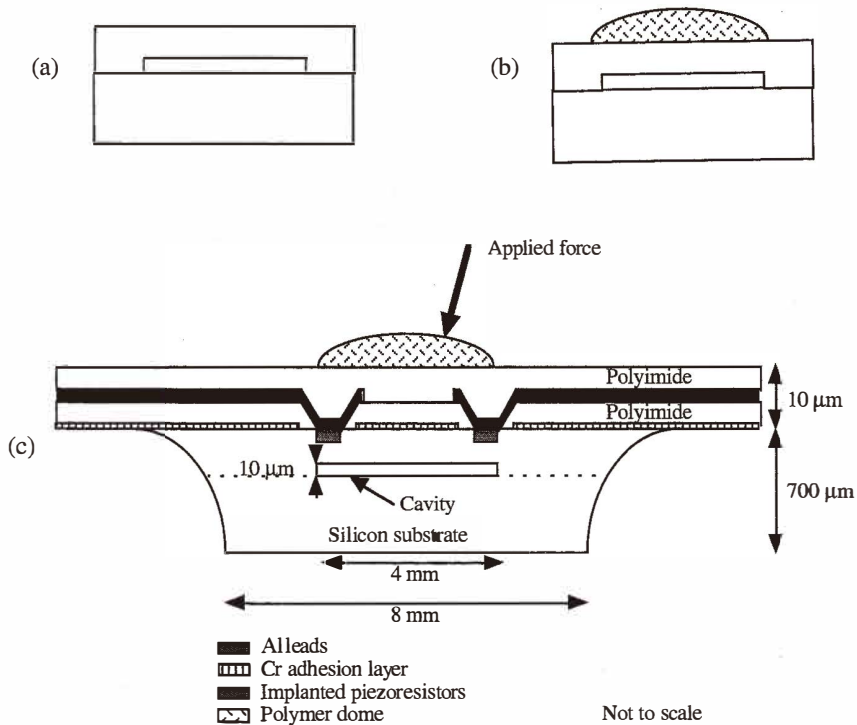


Fig. 1. (a) A pressure sensor based on silicon-to-silicon bonding. (b) The addition of a solid dome converts the pressure sensor into a force sensor. (c) A cross section of the sensing island. The force is applied to the dome, which acts as a force transmission structure.

tains the sensing element. Figure 2 shows a top and a side view of the complete packaged sensor.

### 3. Discussion

#### 3.1 Analytical solution

The analytical solution is a tool that enables estimation of the starting point for model construction. For a specified force range, estimates of diaphragm thickness, displacement and performance can be made using the analytical solution. The solution used is for symmetric bending of circular plates with clamped edges.<sup>(17)</sup> In order to formulate the solution, the plate considered is assumed to be isotropic, linearly elastic, and thin with constant thickness. In addition, geometry, loads and supports are all assumed to be axially symmetric. A final assumption is that deflections are small; specifically, the deflections must be less than a few tenths of the plate thickness such that the load is carried by bending

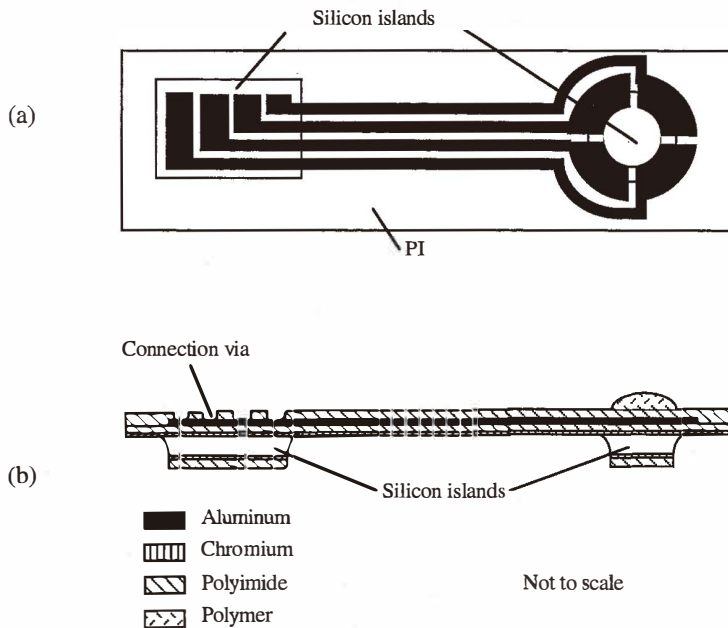


Fig. 2. A complete illustration of the sensor after fabrication. The entire sensor is encased in a layer of polyimide to make the leads flexible and durable. (a) top view and (b) side view.

only. The solution begins with the stresses in the plate created by an applied load that in turn creates moments. Stress equations are used to infer the electrical performance of the sensor. The stresses can be directly related to the change in resistance of the piezoresistors.<sup>(17)</sup> Figure 3 illustrates the radial and tangential stresses calculated from the stress equations. The plot in Fig. 3 shows that the radial stress is at its maximum at the diaphragm edge. Therefore, the diaphragm edge is considered to be the best place for implanting resistors since higher stresses yield greater output sensitivity. Another important piece of information that can be obtained from the plot is that the radial stress is greater than the tangential stress.

Solving for the displacement of a circular plate for the diaphragm displacement over a range of pressures ( $P_0$ ) results in a line with constant slope.<sup>(17)</sup> The slope of the line is dependent on the cube of the diaphragm thickness. The analytical solution can be used to infer a rough idea of the diaphragm thickness needed to provide a given displacement for a given pressure or to provide over force protection at a given pressure.

The analytical solution, being quick and simple, enables estimation of the starting point for model construction. At best, the analytical solution gives an estimation of the necessary diaphragm thickness and can only show stresses in the diaphragm that are based on assumptions needed to solve the equation. For this reason, more realistic solutions are needed. Finite element modeling provides such a solution.

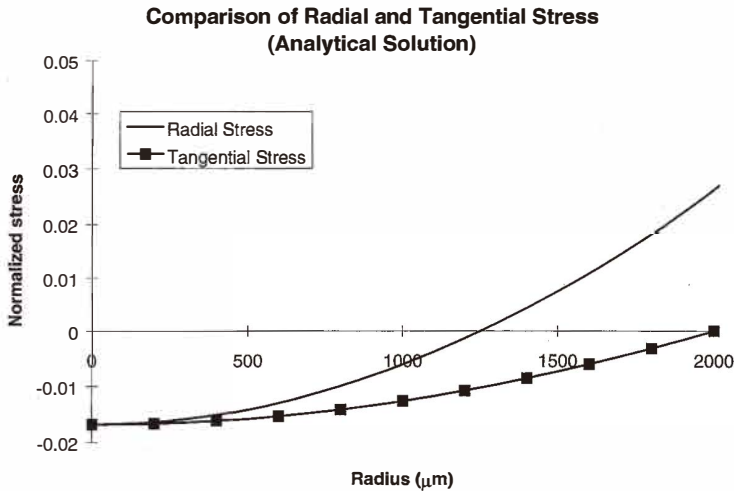


Fig. 3. Comparison of tangential and radial stresses in the clamped edge diaphragm. The stress is normalized; thus the tangential stress is zero at the diaphragm edge.

### 3.2 Finite element modeling (FEM)

Finite element modeling is used to find answers to problems where the geometry is complex or where the boundary conditions are irregular. The FEM method can also solve a three-dimensional model to which asymmetrical load patterns are applied. This is an advantage of FEM over the analytical solution since the analytical solution assumes that all load patterns in a problem are symmetrical. Although the assumption of symmetrical load patterns is convenient for calculations, they are unrealistic when studying tactile sensors. Hence, the FEM method yields more accurate and applicable results than the analytical solution.

Recall that one drawback of the analytical solution was the number of assumptions needed in order to solve the problem. FEM does not require the assumption that the diaphragm is made of one material, nor does it assume that the edges are rigidly clamped. The analytical solution is also limited in that it assumes thin diaphragms, whereas the forces present in tactile sensors present a need for thick diaphragms and shallow cavities. Previously, axisymmetric finite element models have been created with thick diaphragms and deep cavities.<sup>(18)</sup> Finite element analysis on a 2-D rubber (skinlike) diaphragm was done by Ricker and Ellis, who used odd-shaped loading patterns and examined shear strain.<sup>(19)</sup> Other stress analysis on pressure sensors has been done and the stress analysis for the models in this paper is based on those early works.<sup>(5,18)</sup>

In this study, FEM is used to create three models. All the models are built to resemble the real sensor to the greatest degree possible. Constant pressure loading is utilized to study the stress in the areas where the resistors are implanted and the displacement of the diaphragm. The key dimensions are the cavity depth, cavity radius and diaphragm

thickness. The models use a diaphragm 200  $\mu\text{m}$  thick with a radius of 2 mm and a cavity depth of 10  $\mu\text{m}$ . Although the desired depth is not always achieved in the actual sensor, measurement is easily made, and thus any variances from the desired 10  $\mu\text{m}$  depth can easily be accounted for. The mechanical properties of silicon and a complete list of other materials used later in this study are included in Table 1. IMAGES (Celestial Software, Berkeley, CA), the software utilized in this research, plots the model on a grid. The user creates a coordinate system, choosing the units for a unit step in the grid. All output is given in units corresponding to the set of values chosen for the coordinate system. To facilitate convergence, the spacing for a unit step in the coordinate system is chosen to be 10  $\mu\text{m}$ . Thus the cavity depth is one space wide on the grid. Three individual models were created using FEM: the axisymmetric model, the 3-D model, and the domed 3-D model. Both comparison to analytical solutions and mesh refinement were used to evaluate the validity of the models. A discussion of each model follows.

### 3.2.1 Axisymmetric model

The axisymmetric model was the first model created on IMAGES. Axisymmetric models have been studied previously, and the difference between previous models and the one used in this study is the aspect ratio between diaphragm thickness and cavity depth.<sup>(18,20)</sup> The first model constructed identified the high-stress areas.<sup>(3)</sup> Figures 4(a) and (b) show the final axisymmetric model. Note the finer mesh structure at the lower diaphragm edge, the high-stress area, shown in Fig. 4(b).

The axisymmetrical model is intended to be an improvement of the analytical solution, and the same general properties as those in the analytical solution (*e.g.*, displacement, over force protection, etc.) are considered. Figure 5 shows that the diaphragm displacement calculated with the analytical solution is 8.74% less than that obtained using the FEM solution because the edges are not rigidly clamped. The first task is to study changes in the diaphragm thickness. Using a constant pressure of 4 MPa and three diaphragm thicknesses of 200, 250 and 300  $\mu\text{m}$ , a 71% difference was found in the displacement of the 200  $\mu\text{m}$  diaphragm compared to that of the 300  $\mu\text{m}$  diaphragm. The thicker diaphragms show less total displacement but respond over a larger pressure range; the tradeoff is a reduction in sensitivity.

An advantage of FEM is that its calculations of stress do not stop at the edge of the diaphragm. Figure 6 is a plot of the stress along the 2000  $\mu\text{m}$  radius of the diaphragm using

Table 1  
Properties of materials used in modeling.

Material	E ( $\text{N}/\mu\text{m}^2$ )	$\rho$ ( $\text{kg}/\mu\text{m}^3$ )	CTE ( $1/^\circ\text{C}$ )	$\nu$	G ( $\text{N}/\mu\text{m}^2$ )
Silicon	$16.98 \times 10^{-2}$	$2.3283 \times 10^{-15}$	$2.3 \times 10^{-6}$	0.066	$7.96 \times 10^{-2}$
Aluminum	$7.2 \times 10^{-2}$	$2.8 \times 10^{-15}$	$23 \times 10^{-6}$	0.33	$2.71 \times 10^{-2}$
Polyimide	$0.8281 \times 10^{-2}$	$1.45 \times 10^{-15}$	$3 \times 10^{-6}$	0.5	$0.276 \times 10^{-2}$
Torlon	$0.517 \times 10^{-2}$	$1.2 \times 10^{-15}$	$20 \times 10^{-6}$	0.5	$0.1723 \times 10^{-2}$

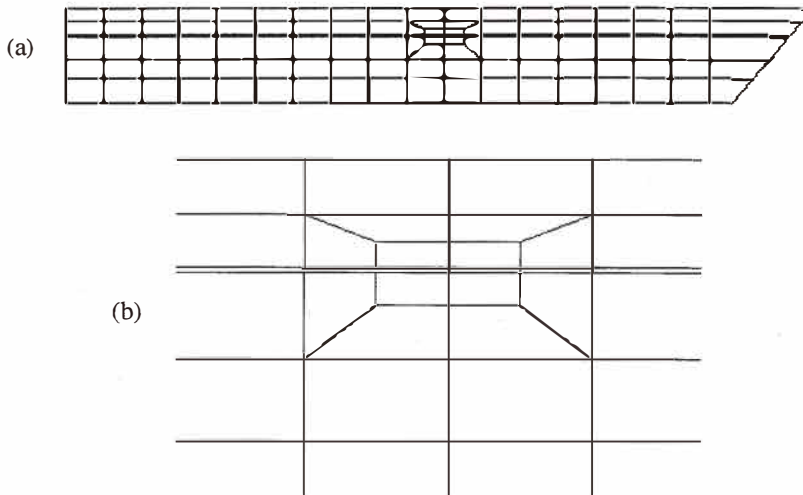


Fig. 4. (a) The axisymmetric model used in this section. (b) A close-up of the edge of the diaphragm where the mesh has been made finer. This figure is also a good representation of the aspect ratio between the gap and the diaphragm. The diaphragm is 20 times thicker than the depth of the cavity.

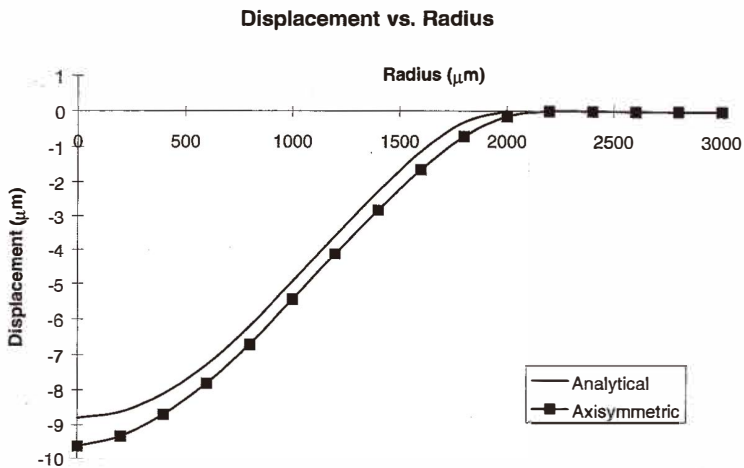


Fig. 5. The displacement of the diaphragm in the analytical solution is 8.74% less at the center of the diaphragm than in the finite element model.

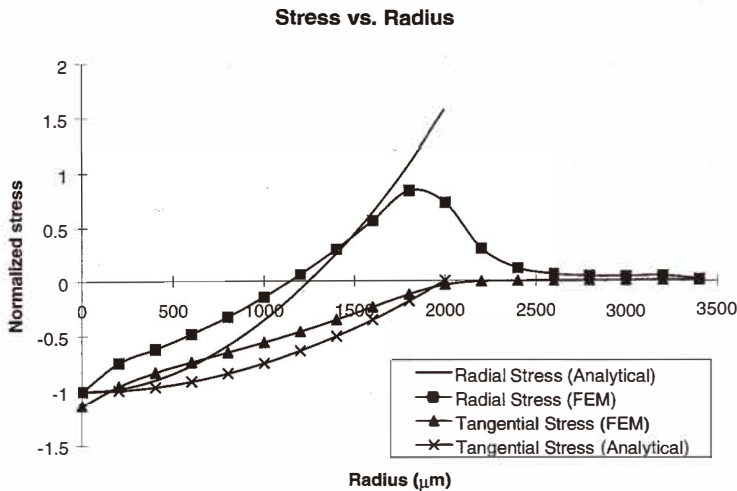


Fig. 6. A quantitative representation of stresses in the axisymmetric model. Note that radial stress is the larger of the two and that a slow rollover of the curve is observed around the diaphragm edge as compared to the analytical solution.

both the FEM method and the analytical solution. The radial stress obtained by the finite element model is nearly constant around the diaphragm edge. This observation is important since it reveals that resistor size can be increased and errors in placement will have a minimal effect on performance.

### 3.2.2 3-D model

More accurate and realistic models are still possible at this point. The models and solutions discussed previously assume the application of a symmetrical load pattern. In order to apply asymmetrical load patterns, it is necessary to create a 3-D model. It is also important to study the effect of pressure increase inside the cavity since the cavity is small and full displacement will increase internal cavity pressure. A large cavity pressure could affect the linearity and output magnitude of the sensor. Figure 7(a) is a top view and Fig. 7(b) a cross-sectional view of the 3-D model without a force transmission structure.

The 3-D models have a similar cross section to the axisymmetric model; however, several differences exist. First, from studies of the axisymmetric model, it can be concluded that the presence of an isotropic etch profile does not change the output significantly. Second, the fine mesh structure around the edge of the diaphragm was simplified for two reasons. The axisymmetric model pinpointed the high-stress area at the diaphragm edge. The axisymmetric model also showed that the fine mesh did not change the magnitude of the stress but only determined its position more precisely. Using a simple structure of evenly sized cubes simplifies the construction of the model without compromising results. The first 3-D model does not include a dome. Several mesh refinements

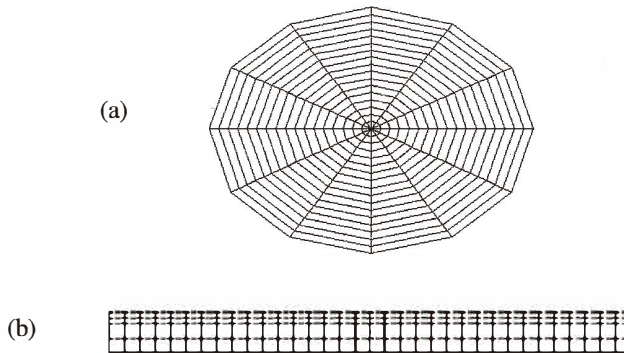


Fig. 7. (a) A top view of the 3-D model without a dome. The model itself is symmetrical, but asymmetrical loads can be applied to it. (b) A cross section of the same model (not to scale). Note that the cavity is so small compared to the diaphragm that it becomes nearly negligible.

were performed with no significant changes in the results leading to the model described here. The model is constructed like a cylinder cut into twelve slices. Each slice is five elements in height with seventeen radial elements for a total of 1104 elements and 1435 nodes. The middle of the cylinder is made up of triangles. All elements use the material properties of silicon. For this model, a  $10\ \mu\text{m}$  thick polyimide layer is added on top of the silicon in order to simulate flexible sensor packaging. This version of the model is used in numerous constant pressure tests. The dome is later added to the top of this model.

This model is important for studying the stresses over the area where the resistors are implanted. The displacement was found to be linear by plotting the displacement of the center of the diaphragm over a range of pressures. From this it can be assumed that the stress over the resistors will also vary linearly with pressure and therefore the voltage from the resistance bridge will also be linear. With this model the displacement exceeds  $10\ \mu\text{m}$  at high pressure and the curve does not rollover as it would if the diaphragm hits a solid substrate. The rollover of the curve expected from the over force protection is not addressed using the model for two reasons. First, in order to accomplish the over force protection, a series of nonlinear springs must be added inside the cavity. Such a nonlinear model makes it very difficult to achieve convergence. Second, since the cavity depth is known precisely, the point that the diaphragm hits the bottom of the cavity can be found either from the graph or by calculation at various pressures. It was found that a pressure of 4 MPa caused a displacement of  $10\ \mu\text{m}$  (the cavity depth).

Figure 8 shows the displacement of the diaphragm along a diameter. The displacement was calculated at a pressure of 4 MPa near the point where the diaphragm bottoms out on the silicon substrate. The displacement is symmetric about the center, with the center being the point of maximum displacement.

The displacement of the diaphragm into the cavity shown in Fig. 8 also reduces the cavity volume. The smaller cavity volume will create an internal pressure pushing up

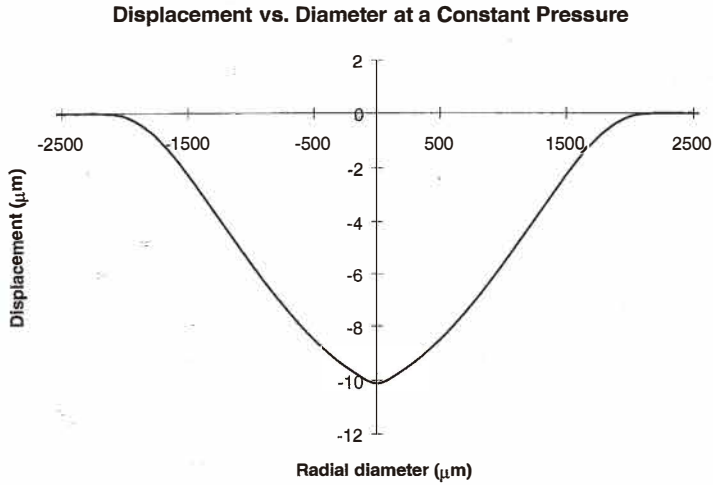


Fig. 8. Curve representing the bottom of the diaphragm at 4 MPa. The volume lost from the cavity is represented by the area under the curve.

against the diaphragm. Thus the differential pressure across the diaphragm will be reduced, as will the total displacement. It is important to observe the effect of internal pressure on sensor output and over force protection. To study this effect, the change in volume must be calculated. In order to accomplish this, an equation for displacement that could be integrated had to be formulated. One method that was considered was curve fitting to the displacement curve. However, it was not utilized because it might not provide an easily integrable equation. The analytical solution is easily integrated and is used to determine the equation that will represent the change in volume. The analytical solution is not exact; however, it gives a measure of the magnitude of the internal change in pressure. The integration in eqs. (1)–(3) is used to calculate the area under the displacement curve ( $dr$ -radial differential,  $dt$ -thickness differential). Differentiating over theta, represents the volume lost in the cavity. Equations (1)–(3) are valid as long as the diaphragm has not bottomed out and are derived from the analytical solution.

$$V = \iiint_{r, t, \theta} z \, dr dt d\theta \quad (1)$$

$$V = \frac{2\pi P_0 t}{64D} \int_r (a^2 - r^2)^2 dr \quad (2)$$

$$V = 1.71 \times 10^{11} \frac{2\pi P_0}{64D} \quad (3)$$

Equation (3) is the volume lost in the cavity at a given pressure. The absolute volume is found by subtracting the result from eq. (3) from the original cavity volume. The original cavity volume can be calculated using the ideal gas law. Initial cavity pressure was assumed to be one atmosphere. The equation can be used to solve for volume at every pressure. Earlier analysis has shown that a  $10\ \mu\text{m}$  (cavity depth) displacement is reached with a pressure of about 4 MPa. Using eq. (3) at this pressure, the internal volume is nearly halved, which implies a doubling of the internal pressure. To compensate for the increase in cavity pressure, the internal pressure can be subtracted from the applied pressure resulting in a new, smaller displacement. A smaller displacement implies less internal pressure which in turn implies an iterative solution. As long as the internal pressure is initially atmospheric, the internal pressure increase is only a small fraction of the applied pressure causing a small but significant effect on the displacement and output from the bridge (4.7% change). The assumption of an initial internal pressure is realistic based on experimental results obtained by Huff *et al.*<sup>(21)</sup>

A key use of this model is the optimization of resistor placement. Figure 9 is a plot of radial and tangential stresses versus the radius. Note the similarity between this plot and the plot of the axisymmetric model (Fig. 6). The only significant difference is that the slope of the radial stress near the center of the diaphragm changes sign. This is assumed to be caused by the triangular elements at the center of the diaphragm. This portion of the model is of little interest in stress analysis since the resistors are located at the edge of the diaphragm and not in the center, and the error can be neglected. The maximum stress at 4 MPa, the point where the diaphragm bottoms out, is at the diaphragm edge and is found to be 48.6 MPa, which is ten times less than the rupture stress of silicon of 360 MPa. The change in resistance is calculated from:

$$\frac{\Delta R}{R} = \pi_{\parallel} \sigma_{\parallel} + \pi_{\perp} \sigma_{\perp}. \quad (4)$$

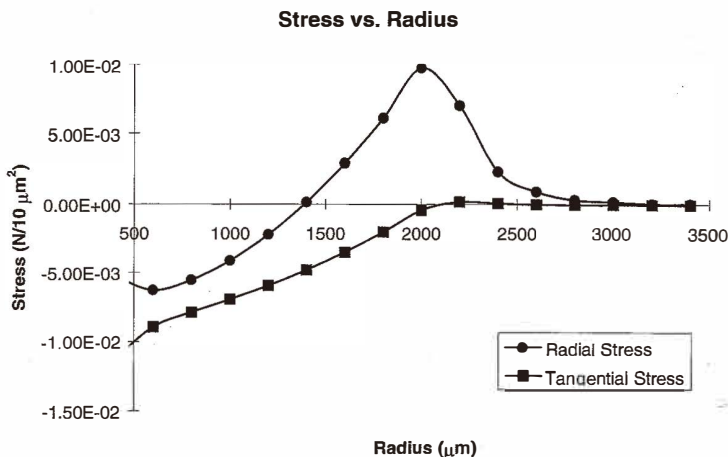


Fig. 9. Radial and tangential stresses along a diaphragm radius.

The values of  $\pi_{\parallel}$  and  $\pi_{\perp}$  are  $-38.5 \times 10^{-4} / \text{MPa}$  and  $40.5 \times 10^{-4} / \text{MPa}$ , respectively.<sup>(5,22)</sup> For the following analysis, the stresses induced under a load of 4 MPa are used. Figure 10 shows the shape and placement of the implanted resistors. The resistors consist of multiple elements of the model. The radial resistor is 5 elements long and two elements wide, while the tangential resistor is three elements wide and two elements long. Each element acts as a series component of the total resistor. The total resistance change can be found by summing each element's resistance change, or the stress can be averaged over the whole resistor and used in eq. (4) to find the resistance change. Table 2 lists the elements along the length direction of the resistors. The stress along any radius is equal, thus elements along the width direction of the resistors will all have the same stresses. The stresses along the length direction must be counted twice during the summation for the radial resistor and three times for the tangential resistor. The stresses over the resistors and the summation of the stress used to find the change in resistance (eq. (4)) are shown in Table 2.

With this information the resistance change ( $\Delta R$ ) for each type of resistor can be calculated, and eqs. (5) and (6) show  $\Delta R$  for the radial and tangential resistors. Using eq. (7), it is possible to calculate the output voltage from the Wheatstone bridge.

$$\alpha = \frac{\Delta R}{R_{\parallel}} = 0.0291 \quad (5)$$

$$\beta = \frac{\Delta R}{R_{\perp}} = 0.0169 \quad (6)$$

$$\frac{\Delta V}{V_{cc}} = \frac{\beta - \alpha}{2 + \alpha + \beta} = -0.119 \quad (7)$$

Combining eqs. (4)–(7) and the total stress from Table 2, the bridge output voltage versus pressure can be calculated. The relationship between voltage and pressure is linear. The voltage is calculated to be zero at 0.1 MPa, and rises to a maximum of 1.1 V at 4 MPa. Next, a 3-D model with a force transmission structure is analyzed.

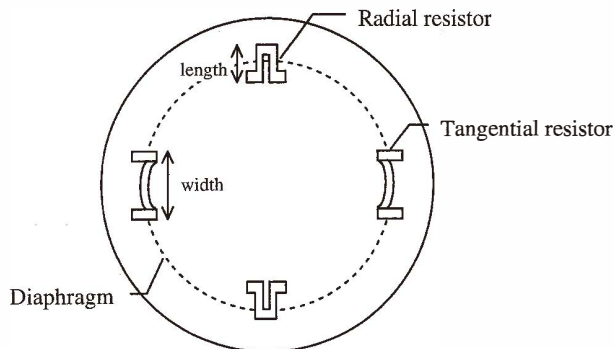


Fig. 10. Shape and placement of the implanted resistors.

Table 2

Stresses over the implanted resistors and the summation for obtaining the total stress. The result is used in eq. (4) to find  $\Delta R$  for the radial and tangential resistors.

Radial Resistor $N/(\mu\text{m})^2$			Tangential Resistor $N/(\mu\text{m})^2$		
Stress			Stress		
Element #	Radial	Tangential	Element #	Radial	Tangential
22	$1.33 \times 10^{-2}$	$-4.82 \times 10^{-1}$	88	$-2.04 \times 10^{-1}$	$6.09 \times 10^{-1}$
23	$2.92 \times 10^{-1}$	$-3.51 \times 10^{-1}$	89	$-4.43 \times 10^{-2}$	$9.71 \times 10^{-1}$
24	$6.09 \times 10^{-1}$	$-2.04 \times 10^{-1}$	90	$1.73 \times 10^{-2}$	$6.99 \times 10^{-1}$
25	$9.71 \times 10^{-1}$	$-4.43 \times 10^{-2}$			
26	$6.99 \times 10^{-1}$	$1.73 \times 10^{-2}$			
Summation	$2.58 \times 10^{-2}$	$-1.08 \times 10^{-2}$	Summation	$-0.231 \times 10^{-3}$	$2.279 \times 10^{-2}$

### 3.2.3 3-D model with a force transmission structure

The force transmission structure is a dome attached to the diaphragm of the sensor in order to negate the effects of physical size (not magnitude) and direction of force. Figure 11 illustrates the finite element mesh of the dome on top of the 3-D model. The effectiveness of the dome is dependent upon the properties of the material chosen, and FEM is utilized to determine the best material. A 3-D model is necessary for examining loading patterns other than uniform pressure. Since the purpose of the dome is to negate the effect of load size, the dome should induce the sensor to give the same output whether it is loaded on top by a 1 mm cylinder or by a 10 mm cylinder, provided that the magnitude of the force is the same. In addition, the effect of load angle will also be reduced by the dome.

The study of domes is integral to the research since the goal is to obtain a force sensor from the pressure sensor. Several different domes were considered: a half sphere, a cross section of a sphere with a known height, and different ellipse shapes. The half sphere was ruled out because its height would have been larger than the thickness of the sensor. For the sensor under consideration, it is necessary to use a dome with a given height and radius equal to the diameter of the diaphragm. The circumference of the dome can be calculated from the equation for a circle. The model for the dome is constructed in much the same way as the sensor itself. The dome has four layers of elements with slanted walls instead of straight ones. Three materials were originally considered for the construction of the domes: aluminum, Torlon and epoxy. Torlon is a synthetic polyamide-imide manufactured by DuPont.<sup>(23)</sup> Aluminum and Torlon have an advantage over epoxy because they can be machined to a desired shape. Epoxy does not have this property; thus, its application and shape would be inconsistent. Exact material properties are known for aluminum and Torlon, but not epoxy. Therefore, Torlon and aluminum domes were modeled and constructed, and epoxy was not considered further.

The object of a force transmission structure is to change a pressure-sensitive device into a force-sensitive device. In order to test this, we apply forces of different shapes and

directions to separate areas of the dome. Figure 12 illustrates the four distinct load cases modeled.

In all four load cases shown in Fig. 12, the displacement and stress profiles were calculated. The goal was to compare results from this model to those obtained from a working sensor. Using the methods detailed in section 3.2.2, the stresses and displacements are used to calculate output voltages for comparison to the prototype sensor output voltages. The forces applied by the cylinder are distributed on the model differently from that of constant pressure loading. The pressure at which the diaphragm bottoms out is known, from which the force on the cylinder is calculated from pressure times area. After determining the magnitude of force, it is necessary to identify which nodes the cylinder impacts. The force is then divided by the number of nodes and the result is applied to each node. This force is the maximum value applied to the model. Smaller forces are also applied to study the displacement and stress profiles. Figure 13 illustrates the results of load cases (a) and (b) (from Fig. 12) for the Torlon dome. There is a small difference in the displacements that could be accounted for by one of two reasons. First, the application of the result of the force divided by the number of nodes is only a first-order approximation of the real force profile. Second, the nodes of the model are not arranged in a pattern like the cylinder applying the force, and therefore the area on which the force is applied is only an



Fig. 11. A cross-sectional view of the finite element mesh including the dome.

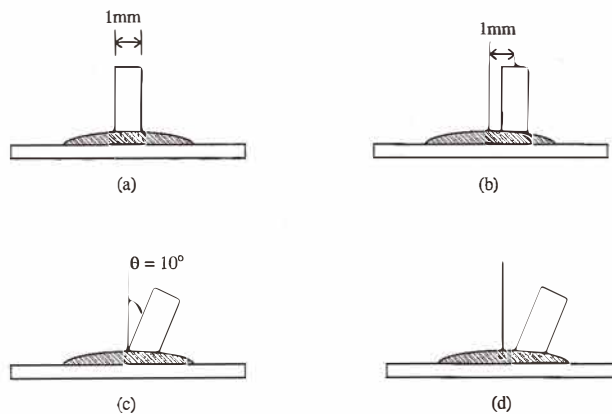


Fig. 12. The four load cases. Equivalent outputs from each verify the force transmission structure. Force is applied to the top of the cylinder.

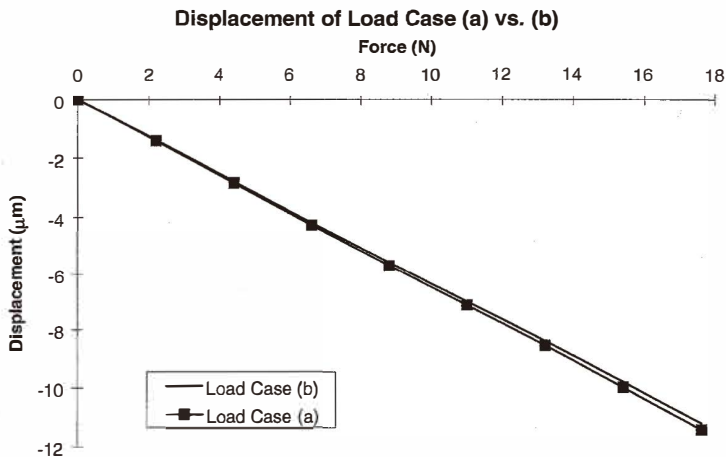


Fig. 13. Comparison of the displacements from load cases (a) and (b) in Fig. 12. The small difference in the displacements was found to hold true in the prototype sensor.

approximation of a circle. The results are similar to the experimental results obtained for a working sensor, where the effect of load location was found to be statistically significant but small (4–9% of the mean sensor output) for the same load case using a prototype sensor.<sup>(7)</sup> Overall the difference in displacements between the load cases is small (about 0.1  $\mu\text{m}$ ), and the displacements can be interpreted as being nearly equal to each other.

In order to apply loads as shown in Fig. 12(c) and (d), the force applied to each node is separated into its normal and tangential components. Each component is applied to the nodes under the cylinder in its respective direction. An evaluation of these cases produced displacements similar to those observed in load cases (a) and (b) (Fig. 12). This also agrees with experimental results, which indicates that the effect of load angle under the same conditions was not statistically significant. Thus, it can be concluded that the sensor is not sensitive to the direction of the applied force. The model of the dome performs nearly perfectly as a force transmission structure.

Finally, the model is used to study the effect of different dome materials. The dome material is dictated by the environment and load to which the sensor will be subjected. Domes of aluminum and Torlon are attached to the 3-D model. The material properties of Torlon and aluminum are given in Table 1. It is found that the model with a Torlon dome bottoms out under a force of 18 N. The aluminum dome can withstand nearly 7 times as much force (about 140 N) before bottoming out.

#### 4. Conclusions

The object of this research is to create a realistic model for a silicon force sensor, which can be used to examine the effects of change in sensor characteristics without the need for a prototype. An analytical solution was studied first. To improve accuracy over an analytical solution, finite element models of the sensor were created. Specifically, axisymmetric and 3-D models with and without force transmission structures were generated using IMAGES software. Each new model produced improved, more realistic results. During the course of the modeling a prototype sensor was fabricated. Figure 14 illustrates a comparison of the analytical solution, the 3-D model with and without internal pressure compensation, and a prototype sensor. One significant difference between the models and the sensor is the rollover of the plot for the prototype sensor, which is caused by the over force protection. As discussed previously, the over force protection originates only from bottoming out the diaphragm, and the internal cavity pressure has been shown to have a negligible effect. A future model may be considered which would include nonlinear springs in the cavity to represent the over force protection. Figure 14 also shows the output voltage of resistors which were misaligned by 200  $\mu\text{m}$  or 400  $\mu\text{m}$ . The alignment method used when fabricating the prototype sensor was crude, and misalignment between the resistors and the diaphragm edge of a few hundred microns exists which causes the discrepancies in the magnitude of the output voltage. Future sensor fabrication with an infrared backside aligner would reduce these alignment errors to less than 5  $\mu\text{m}$  and allow for a better comparison to the FEM model.

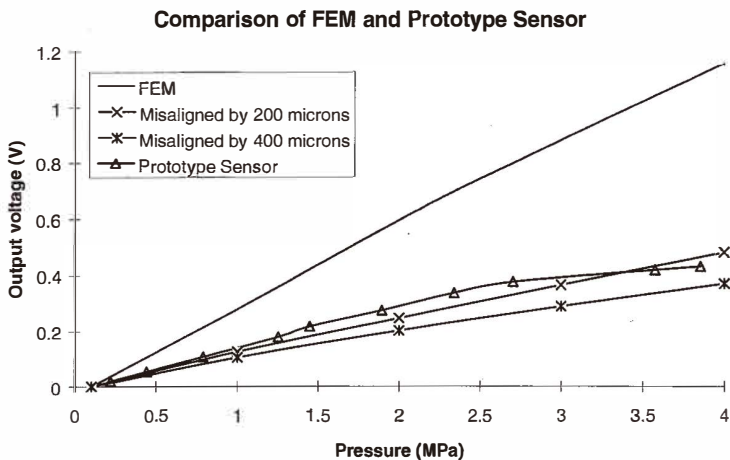


Fig. 14. A comparison of the output voltage from the 3-D FEM, the output from misaligned resistors, and the output obtained from a prototype sensor. All outputs were obtained at a constant pressure load.

The role of the force transmission structure is to transmit different loads evenly over the sensing area. The dome modeled achieved this purpose well. From this study, it can be concluded that FEM effectively predicts the necessary properties of a tactile sensor with a designated purpose. Specifically, the sensor has a linear output, and equivalent loads produce equivalent outputs regardless of the placement of the load. The sensor also has adequate protection against over force.

### Acknowledgement

A portion of this work was completed while the authors were in the Department of Electrical and Computer Engineering at the University of Wisconsin at Madison.

### References

- 1 P. M. Sarro: Sensors and Actuators **A 31** (1992) 138.
- 2 S. Omata and Y. Terunuma: Sensors and Actuators **A 35** (1992) 9.
- 3 D. J. Beebe: Dissertation: University of Wisconsin Madison, 1993.
- 4 O. Tufté, P. Chapman and D. Long: Journal of Applied Physics **33** (1961) 3322.
- 5 S. Clark and K. Wise: IEEE Transactions on Electron Device **ED-26** (1979) 1887.
- 6 L. Christel, K. Petersen, P. Barth, F. Pourahmadi, J. Mallon and J. Bryzek: Sensors and Actuators **A 21-23** (1990) 84–88.
- 7 D. J. Beebe, A. Hsieh, D. Denton and R. Radwin: Sensors and Actuators **A 50** (1995) 55.
- 8 W. Ko, J. Hyncecek and S. Boettcher: IEEE Transactions on Electron Devices **ED-26** (1979) 1896.
- 9 J. Sorab, R. H. Allen and B. Gonik: IEEE Transactions on Biomedical Engineering **35** (12) (1988) 1090.
- 10 H. Tilmans and S. Bouwstra: Journal of Micromechanical Microengineering **3** (1993) 192.
- 11 K. Ikeda, H. Kuwayama, T. Kobayashi, T. Watanabe, T. Nishikawa, T. Yoshida and K. Harada: Sensors and Actuators **A 23** (1990) 1007.
- 12 L. Liu, X. Zheng and Z. Li: Sensors and Actuators **A 32** (1993) 193.
- 13 S. Sugiyana, K. Kawahata, M. Yoneda and I. Igarashi: Sensors and Actuators **A 21-23** (1990) 397–400.
- 14 D. J. Beebe and D. D. Denton: Sensors and Actuators **A 44** (1994) 57.
- 15 K. Petersen, P. Barth, J. Poydock, J. Brown, J. M. Jr. and J. Bryzek: Proc. IEEE Solid-State Sensor and Actuator Workshop, Hilton Head Island, SC (1988) 144.
- 16 Y. Wang, L. Liu, X. Zheng and Z. Li: Sensors and Actuators **A 21-22** (1990) 62–64.
- 17 R. D. Cook and W. C. Young: Advanced Mechanics of Materials (1985).
- 18 A. Yasukawa, S. Shimada, Y. Matsuoka and Y. Kanda: Japanese Journal of Applied Physics **21** (1982) 1049.
- 19 S. Ricker and R. Ellis: Proceedings of the IEEE International Conference on Robotics and Automation (1993).
- 20 T. Speeter: The Interactive Journal of Robotics Research **11** (1992) 1.
- 21 M. A. Huff, A. D. Nikolich and M. A. Schmidt: J. Microelectroelectrical Systems **2** (1993) 74.
- 22 A. Yasukawa, M. Shimazoe and Y. Matsuoka: IEEE Transactions on Electron Devices **36** (1989) 1295.
- 23 DuPont: Kapton-Summary of Properties (1988).